ATLAS Paper Draft

TOPQ-2020-03

Version 1.0

Target journal: JHEP

Comments are due by: 08 May 2020

Supporting internal notes

Measurements of inclusive and differential cross-sections of $t\bar{t}\gamma$ production in $e\mu$ final states at 13 TeV with the ATLAS detector: https://cds.cern.ch/record/2674026

Measurements of inclusive and differential cross-sections of $t\bar{t}\gamma$ and $tW\gamma$ production in the $e\mu$ channel at 13 TeV with the ATLAS detector

Inclusive and differential cross-sections for the production of top quarks in association with a photon are measured with proton-proton collision data corresponding to an integrated luminosity of $139\,\mathrm{fb}^{-1}$. The data were collected by the ATLAS detector at the LHC during Run 2 between 2015 and 2018 at a centre-of-mass energy of 13 TeV. The measurements are performed in a fiducial volume defined at parton level. Events with exactly one photon, one electron and one muon of opposite sign, and at least two jets, out of which at least one is b-tagged, are selected. The fiducial cross-section is measured to be $39.6\,^{+2.7}_{-2.3}$ fb. Differential cross-sections as functions of several observables are compared to state-of-the-art Monte Carlo simulations and next-to-leading order theoretical calculations. These include cross-sections as functions of the photon transverse momentum and absolute pseudorapidity and angular variables related to the photon and the leptons and between the two leptons in the event. All measurements are in agreement with the predictions.

Document created on 27th April 2020 using ATLAS LATEX Version 08-02-00.

Analysis Team

[*email:* atlas-TOPQ-2020-03-editors@cern.ch]

Ivor Fleck, Arnulf Quadt, Elizaveta Shabalina, Yichen Li, Knut Zoch, John Kamal Rizk
Meshreki, Steffen Korn, Amartya Rej, Thomas Peiffer, Carmen Diez Pardos

Editorial Board

[*email:* atlas-TOPQ-2020-03-editorial-board@cern.ch]

Marina, Cobal (Udine) (chair)
Thorsten, Kuhl (DESY)
Kazuya, Mochizuki (Montreal)

Measurements of inclusive and differential cross-sections of $t\bar{t}\gamma$ and $tW\gamma$ production in the $e\mu$ channel at 13 TeV with the ATLAS detector

The ATLAS Collaboration

Inclusive and differential cross-sections for the production of top quarks in association with a photon are measured with proton-proton collision data corresponding to an integrated luminosity of 139 fb^{-1}. The data were collected by the ATLAS detector at the LHC during Run 2 between 2015 and 2018 at a centre-of-mass energy of 13 TeV. The measurements are performed in a fiducial volume defined at parton level. Events with exactly one photon, one electron and one muon of opposite sign, and at least two jets, out of which at least one is b-tagged, are selected. The fiducial cross-section is measured to be 39.6 $^{+2.7}_{-2.3}$ fb. Differential cross-sections as functions of several observables are compared to state-of-the-art Monte Carlo simulations and next-to-leading order theoretical calculations. These include cross-sections as functions of the photon transverse momentum and absolute pseudorapidity and angular variables related to the photon and the leptons and between the two leptons in the event. All measurements are in agreement with the predictions.

1 Introduction

Precise measurements of top-quark production and decay properties provide crucial information for testing the expectations of the Standard Model (SM) and its possible extensions. In particular, the study of the associated production of a top-quark pair ($t\bar{t}$) with a photon probes the $t\gamma$ electroweak coupling. Furthermore, measurements of the inclusive and differential cross-sections of this process are of particular interest because these topologies are sensitive, for instance, to new physics through anomalous dipole moments of the top quark [1–3] and in the context of effective field theories (EFT) [4].

First evidence for the production of $t\bar{t}$ in association with a photon ($t\bar{t}\gamma$) was reported by the CDF Collaboration [5], while the observation of the $t\bar{t}\gamma$ process was established by the ATLAS Collaboration in proton-proton (pp) collisions at $\sqrt{s}$ = 7 TeV [6]. Both the ATLAS and CMS Collaborations measured the $t\bar{t}\gamma$ cross-section at $\sqrt{s}$ = 8 TeV [7, 8]. First measurements of the inclusive and differential cross-sections at $\sqrt{s}$ = 13 TeV were performed by the ATLAS Collaboration [9].

This paper presents a measurement of the fiducial inclusive and differential $t\bar{t}\gamma$ production cross-sections in the final state with one electron and one muon, referred to as the $e\mu$ channel. Events where the electrons and muons arise from the leptonic decays of τ-leptons are excluded. The measurement is performed using the full data set recorded at the LHC between 2015 and 2018 at a centre-of-mass energy of $\sqrt{s}$ = 13 TeV and corresponding to an integrated luminosity of 139 fb^{-1}. The fiducial inclusive cross-section is measured using a likelihood fit to the distribution of S_{T}, defined as the scalar sum over all transverse momenta in the event, including leptons, photons, jets and missing transverse momentum. The differential cross-sections, absolute and normalised to unity, are measured in the same fiducial region as the inclusive cross-section, as functions of photon kinematic variables, angular variables related to the photon and the leptons, and angular separations between the two leptons in the event.

Compared to the previous $t\bar{t}\gamma$ ATLAS analysis with 13 TeV data [9], only the $e\mu$ channel is considered since it provides a clean final state with a small background contribution and, thus, no multivariate analysis techniques are needed to separate signal and background processes. Additionally, the cross-sections are measured at the parton level rather than the particle level to be compared to the theory calculation in Refs. [10, 11]. The calculation constitutes the first full computation for $t\bar{t}$ production with a final-state photon in hadronic collisions at next-to-leading order (NLO) in quantum chromodynamics (QCD), $pp \rightarrow bWbW\gamma$, including all resonant and non-resonant diagrams, interferences, and off-shell effects of the top quarks and the W bosons. Therefore, in this paper the combined $t\bar{t}\gamma + tW\gamma$ production cross-section is measured, referred to as signal in the following.

The paper is organised as follows. The ATLAS detector is briefly introduced in Section 2. Details of the event-simulation generators and their theoretical predictions are given in Section 3. The object and event selection and the analysis strategy are presented in Sections 4 and 5. The systematic uncertainties are described in Section 6. The results for the inclusive and differential cross-sections are presented in Sections 7 and 8, respectively. Finally, a summary is given in Section 9.

2 ATLAS detector

ATLAS [12–14] is a multipurpose detector with a forward–backward symmetric cylindrical geometry with respect to the LHC beam axis [1]. The innermost layers consist of tracking detectors in the pseudorapidity range $|\eta| < 2.5$. This inner detector (ID) is surrounded by a thin superconducting solenoid that provides a 2 T axial magnetic field. It is enclosed by the electromagnetic and hadronic calorimeters, which cover $|\eta| < 4.9$. The outermost layers of ATLAS consist of an external muon spectrometer (MS) within $|\eta| < 2.7$, incorporating three large toroidal magnetic assemblies with eight coils each. The field integral of the toroids ranges between 2.0 and 6.0 Tm for most of the acceptance. The MS includes precision tracking chambers and fast detectors for triggering. A two-level trigger system [15] reduces the recorded event rate to an average of 1 kHz.

3 Signal and background modelling

The estimation of signal and background contributions relies on the modelling of these processes with simulated events produced with Monte Carlo (MC) event generators. The response of the ATLAS detector is simulated [16] with GEANT4 [17]. For some of the estimates of modelling uncertainties, the fast-simulation package AtlFast-II is used instead of the full detector simulation. Additional pp interactions from the same bunch crossing (pile-up) are generated with PYTHIA 8 [18, 19] using the set of tuned parameters called A2 [20] and the MSTW2008LO parton distribution functions (PDF) set [21]. Corrections derived from dedicated data samples are applied to the MC simulation to improve the agreement with data.

This analysis uses both *inclusive* samples, in which processes are generated at matrix-element (ME) level without explicitly including a photon in the final state, and *dedicated* samples, where photons are included in the ME level generation step. Dedicated samples with a photon in the ME are generated for the $t\bar{t}\gamma$ and $tW\gamma$ final states, as well as for $V\gamma$ processes with additional jets. Here, V denotes either a W or a Z boson. Although no photons are generated at ME level in the inclusive samples, radiation of photons is still accounted for by the showering algorithm. Combining inclusive and dedicated samples for the modelling of processes might result in double-counting photon radiation in certain phase-space regions.

As a consequence, an overlap-removal procedure is performed between inclusive and dedicated samples. Photon radiation simulated at ME level in dedicated samples achieves higher accuracy than the photon radiation in the showering algorithm. On the other hand, kinematic requirements are applied to the kinematic properties of the photons at ME level in the dedicated samples. In the overlap-removal procedure, all events from the dedicated samples are kept while events from the inclusive samples are discarded if they contain a parton-level photon that fulfils the kinematic requirements of the dedicated sample of $p_\text{T}(\gamma) > 15$ GeV and $\Delta R(\gamma, \ell) > 0.2$, where $p_\text{T}(\gamma)$ is the photon's transverse momentum and $\Delta R(\gamma, \ell)$ is the angular distance between the photon and any charged lepton.

The dedicated sample for the $t\bar{t}\gamma$ signal process is simulated using the MADGRAPH5_aMC@NLO generator (v2.33) [22] and the NNPDF2.3LO PDF set [23] at leading order (LO) in QCD. The events are generated as a doubly-resonant $2 \rightarrow 7$ process, as e.g. $pp \rightarrow b\ell\nu b\ell\nu\gamma$, and, thus, diagrams where the photon is radiated

---

[1] ATLAS uses a right-handed coordinate system with its origin at the nominal interaction point (IP) in the centre of the detector and the z-axis along the beam pipe. The x-axis points from the IP to the centre of the LHC ring, and the y-axis points upwards. Cylindrical coordinates (r, ϕ) are used in the transverse plane, ϕ being the azimuthal angle around the z-axis. The pseudorapidity is defined in terms of the polar angle θ as $\eta = -\ln\tan(\theta/2)$. Angular distance is measured in units of $\Delta R \equiv \sqrt{(\Delta\eta)^2 + (\Delta\phi)^2}$.

from the initial state (in case of quark-antiquark annihilation), intermediate top quarks, the b-quarks, the intermediate W bosons as well as the decay products of the W bosons are included. The photon is required to have $p_T > 15$ GeV and $|\eta| < 5.0$ and the leptons to satisfy $|\eta| < 5.0$. The ΔR between the photon and any of the charged particles among the seven final-state particles are required to be greater than 0.2. The top-quark mass in this and all other samples is set to 172.5 GeV. The renormalisation and the factorisation scales are set to $0.5 \times \sum_i \sqrt{m_i^2 + p_{T,i}^2}$, where the sum runs over all the particles generated from the ME calculation. The event generation is interfaced to Pythia 8 (v8.212) using the A14 tune [24] to model parton shower, hadronisation, fragmentation and underlying event. Heavy-flavour hadron decays are modelled with EvtGen [25]; this programme is used for all samples, except for those generated using the Sherpa MC programme.

Two dedicated samples for the $tW\gamma$ process are generated with the MadGraph5_aMC@NLO generator as well. The first one is produced at LO in the five-flavour scheme for the $2 \rightarrow 3$ process assuming a stable top quark. The second set of events is generated as a $2 \rightarrow 6$ process in the five-flavour scheme, where the photon is radiated from any other charged final state particle. The two sets of events are complementary and, once combined, provide a full simulation of the $tW\gamma$ process. Both samples make use of the NNPDF2.3LO PDF set and are interfaced to Pythia 8 (v8.212) for the showering using the A14 tune. The photon is also required to have $p_T > 15$ GeV and $|\eta| < 5.0$ and to be separated by $\Delta R > 0.2$ from any parton. At NLO, the $tW\gamma$ process interferes with the $t\bar{t}\gamma$ signal process when including the spectator b-quark and would contribute to the off-shell part of the signal. Also the theoretical cross-section calculation for the $pp \rightarrow bWbW\gamma$ process from Refs. [10, 11] includes the off-shell contribution. Although possible interference effects between $t\bar{t}\gamma$ and $tW\gamma$ are still missing in the simulated LO samples, the $tW\gamma$ process is treated as part of the signal in this analysis.

Events with $W\gamma$ and $Z\gamma$ final states (with additional jets) are simulated as dedicated samples. $W\gamma$ processes are simulated with Sherpa 2.2.2 [26, 27] at NLO accuracy in QCD using the NNPDF3.0NNLO PDF set, whereas $Z\gamma$ events are generated with Sherpa 2.2.4 at LO in QCD. The samples are normalised to the cross-sections given by the corresponding MC simulation. The Sherpa generator performs all steps of the event generation, from the hard process to the observable particles. All samples are matched and merged by the Sherpa-internal parton showering based on Catani-Seymour dipoles [28, 29] using the MEPS@NLO prescription [30–32]. Virtual corrections for the NLO accuracy in QCD in the matrix element are provided by the OpenLoops library [33, 34].

Inclusive $t\bar{t}$ production processes are simulated at matrix-element level at NLO accuracy in QCD using Powheg-Box-v2 [35–37]. The calculation uses the NNPDF3.0NLO PDF set [38]. The parton shower is generated with Pythia 8 (v8.230), for which the A14 tune is used. The $t\bar{t}$ events are normalised to a cross-section value calculated with the Top++2.0 programme at next-to-next-to-leading order (NNLO) in perturbative QCD, including soft-gluon resummation to next-to-next-to-leading-logarithm order (see Ref. [39] and references therein).

Events with inclusive W- and Z-boson production in association with additional jets are simulated with Sherpa 2.2.1 [26, 27] at NLO in QCD. The NNPDF3.0NLO PDF set is used in conjunction with a dedicated tune provided by the Sherpa authors. The samples are normalised to the NNLO cross-section in QCD [40].

Events with two vector bosons, that is, WW, WZ and ZZ, are generated with Sherpa versions 2.2.2 (purely leptonic decays) and 2.2.1 (all others) at LO in QCD. The NNPDF3.0NNLO PDF set is used in conjunction with a dedicated tune provided by the Sherpa authors. The samples are normalised to NLO accuracy cross-sections in QCD [41].

Events with a $t\bar{t}$ pair and an associated W or Z boson ($t\bar{t}V$) are simulated at NLO ME level with MadGraph5_aMC@NLO using the NNPDF3.0NLO PDF set. The ME generator is interfaced to Pythia 8 (v8.210), for which the A14 tune is used in conjunction with the NNPDF2.3LO PDF set. The samples are normalised to NLO in QCD and electroweak theory [42].

The background processes are sorted in three categories based on the origin of the reconstructed photon required in the event selection. All three are estimated based on MC simulation by categorising events from all considered MC samples that are not classified as signal events. They include processes without prompt photons like $t\bar{t}$, W+jets, Z+jets, diboson and $t\bar{t}V$ production, as well as background processes with an additional prompt photon. The first category is labelled *h-fake* and contains any type of hadronic fakes that mimic a photon signature in the detector. This category includes photon signatures faked by hadronic energy depositions in the electromagnetic calorimeter, but also hadron decays involving photons, for example $\pi^0 \to \gamma\gamma$ decays. It also includes processes with a prompt photon, where the prompt photon is not reconstructed in the detector or does not pass the selection requirements, but a h-fake photon does. Studies performed with data-driven techniques show that possible data-driven corrections have a negligible effect on the shape of relevant observables. Possible differences in the total expected number of events are covered by a normalisation uncertainty as described in Section 6. The *e-fake* category contains processes with an electron mimicking a photon signature in the calorimeter. Similar to the h-fake category, this category includes contributions from processes without a prompt photon but an e-fake photon as well as processes with a prompt photon in the simulation, but an e-fake photon in the reconstruction. This category represents a minor background contribution. The third category is called *prompt γ background* and contains any type of background process with a prompt photon. The background contribution from $t\bar{t}$ production with a photon produced in an additional pp interaction in the same bunch crossing is found to be negligible.

$t\bar{t}\gamma$ and $tW\gamma$ events where one or both W bosons decay into τ-leptons, which then subsequently decay into e or μ, are categorised as *Other $t\bar{t}\gamma/tW\gamma$*, and not as $e\mu$ signal, following the definition of signal events in the theory calculation in Refs. [10, 11]. Single-lepton events, where a second lepton is faked by hadronic energy depositions, are also included in the category *Other $t\bar{t}\gamma/tW\gamma$*. The contribution of $t\bar{t}\gamma$ single-lepton events was found to be negligible in the $e\mu$ final state in the previous measurement [9] and it is therefore estimated from the MC simulation.

4 Event selection

The data set used in this analysis corresponds to the 139 fb^{-1} of integrated luminosity collected with the ATLAS detector during the Run 2 period. Each event in data and simulation is required to have at least one reconstructed primary vertex with at least two associated reconstructed tracks. Furthermore, only events where at least one of the single-electron [43] or single-muon triggers was fired are selected. The p_{T} threshold of the single-lepton triggers was increased over the different data-taking periods from 25 GeV in 2015 to 27 GeV in 2016 to 28 GeV in 2017 and 2018.

The main physics objects considered in this analysis are electrons, muons, photons, jets, b-jets and missing transverse momentum. Electrons are reconstructed from energy deposits in the electromagnetic calorimeter associated with reconstructed tracks in the ID system. They are identified with a combined likelihood technique [44] and are required to be isolated. The origin of the electron track has to be compatible with the

176 primary vertex. Electrons are calibrated with the method described in Ref. [44]. They are selected if they
177 fulfil $p_T > 25$ GeV and $|\eta_{\mathrm{clus}}| < 2.47$, excluding the calorimeter crack region $1.37 < |\eta_{\mathrm{clus}}| < 1.52$.[2]

178 Muons are reconstructed with a combined algorithm, using the track segments in the various layers of
179 the muon spectrometer and the tracks in the ID system. The reconstruction, identification and calibration
180 methods are described in Ref. [45]. Only isolated muons with calibrated $p_T > 25$ GeV and $|\eta| < 2.5$ are
181 considered. The muon track is also required to originate from the primary collision vertex.

182 Photons are reconstructed from energy deposits in the central region of the electromagnetic calorimeters.
183 If the cluster is considered not matched to any reconstructed track in the ID system, the photon candidate
184 is classified as unconverted. If the cluster is matched with one or two reconstructed tracks that are
185 consistent with originating from a photon conversion and if, in addition, a conversion vertex can be
186 found, the photon candidate is classified as converted. Both kinds of photons are considered in this
187 analysis. Photons are reconstructed and identified as described in Ref. [46] and the energies are calibrated
188 with the method described in Ref. [47]. They are also subject to an isolation requirement defined as
189 $E_T^{\mathrm{iso}}\big|_{\Delta R < 0.4} < 0.022 \cdot E_T(\gamma) + 2.45$ GeV in conjunction with $p_T^{\mathrm{iso}}\big|_{\Delta R < 0.2} < 0.05 \cdot E_T(\gamma)$, where E_T^{iso} refers
190 to the calorimeter isolation within $\Delta R < 0.4$ in the direction of the photon candidate and p_T^{iso} is the track
191 isolation within $\Delta R < 0.2$. Only photons with calibrated $E_T > 20$ GeV and $|\eta_{\mathrm{clus}}| < 2.37$, excluding the
192 calorimeter crack region $1.37 < |\eta_{\mathrm{clus}}| < 1.52$, are considered.

193 The jets are reconstructed using the anti-k_t algorithm [48] in the FASTJET implementation [49] with a
194 distance parameter $R = 0.4$ (in the η-ϕ plane). They are reconstructed from topological calorimeter
195 clusters [50]. The jet energy scale and jet energy resolution are calibrated using information from both
196 simulation and data [51]. The jets are required to have $p_T > 25$ GeV and $|\eta| < 2.5$. In order to reject jets
197 from pile-up or other primary vertices, candidates for such jets are identified with the *Jet Vertex Tagger* [52]
198 and rejected.

199 The *b*-tagging algorithm to identify jets from *b*-quark hadronisation [53] is based on a boosted decision
200 tree combining information from other algorithms utilising the track impact parameter, secondary vertices,
201 and a multi-vertex reconstruction algorithm. A working point with an efficiency of 85% on simulated $t\bar{t}$
202 events is used, corresponding to rejection factors for charm quark and light-flavour parton initiated jets of
203 3.1 and 35, respectively. The flavour tagging efficiency of *b*-jets as well as of *c*- and light-jets is calibrated
204 as described in Ref. [54].

205 The reconstructed missing transverse momentum E_T^{miss} [55] is computed as the negative vector sum over
206 all reconstructed, fully calibrated physics objects including photons and remaining unclustered energy, also
207 called *soft term*. This soft term is estimated from low-p_T tracks associated with the primary vertex not
208 being assigned to any reconstructed object.

209 An overlap removal procedure is applied to avoid the reconstruction of the same energy clusters or tracks
210 as different objects. First, electron candidates sharing their track with a muon candidate are removed and
211 jets within a $\Delta R = 0.2$ cone of a remaining electron are excluded. Secondly, electrons within a $\Delta R = 0.4$
212 cone of the remaining jets are removed. If the distance between a jet and any muon candidate is $\Delta R < 0.4$,
213 the muon candidate is discarded if the jet has more than two associated tracks, otherwise the jet is removed.
214 Finally, photons within a $\Delta R = 0.4$ cone of a remaining electron or muon are removed and the jets within a
215 $\Delta R = 0.4$ cone of a remaining photon are excluded.

216 Events are selected with exactly one electron and exactly one muon, each of which must carry $p_T > 25$ GeV.
217 At least one of these leptons has to be matched to a fired single-lepton trigger and has to fulfil the respective

---

[2] η_{clus} denotes the pseudorapidity of the calorimeter cluster associated with the electron.

Table 1: Event yields before the likelihood fit for data, the signal, and background processes after the full selection. All categories are estimated based on MC simulation including correction factors for detector effects as described in Section 6. The combination of all $t\bar{t}\gamma$ and $tW\gamma$ categories is scaled to match the event yields in data. The quoted uncertainties correspond to the total statistical and systematic uncertainties (cf. Section 6) added in quadrature.

	Events
$t\bar{t}\gamma$ $e\mu$	2391 ± 130
$tW\gamma$ $e\mu$	156 ± 15
Other $t\bar{t}\gamma/tW\gamma$	279 ± 15
h-fake	78 ± 40
e-fake	23 ± 12
Prompt γ bkg.	87 ± 40
Total	3014 ± 160
Data	3014

p_T threshold of the trigger. Electrons and muons must have opposite sign charges and the $e\mu$ invariant mass is required to be higher than 15 GeV. The event is required to have at least two jets and at least one of the jets must be b-tagged. In addition, all events must contain exactly one reconstructed photon fulfilling the condition that ΔR between the selected photon and any of the leptons is greater than 0.4.

The observed and pre-fit event yields after selection are listed in Table 1 for the different signal and background categories described in Section 3. The combination of all $t\bar{t}\gamma$ and $tW\gamma$ categories is normalised to match the event yields in data for illustration, since the measurements are independent of the pre-fit normalisation of the signal and *Other $t\bar{t}\gamma/tW\gamma$* events. Correction factors for detector effects (described in Section 6) are applied, when needed, to improve the description of the data by the simulation.

The modelling of signal and background is inspected through the comparison of distributions. A selection of these distributions showing a comparison between the MC simulation before the likelihood fit and data is presented in Figure 1. The combination of all $t\bar{t}\gamma$ and $tW\gamma$ categories is normalised to match the event yields in data as done in Table 1 to illustrate the good description of the shape of the different kinematic variables. All systematic uncertainties that are introduced in Section 6 are included in these distributions and their quadratic sum is illustrated by the shaded error bands. The uncertainties cover almost all discrepancies observed between data and simulations.

5 Analysis strategy

The inclusive and differential cross-sections are measured in the fiducial region described in Section 5.1 and the same strategy for the estimation of the background contributions and systematic uncertainties is followed. In the inclusive cross-section the S_T distribution is fitted and the post-fit background yields and systematic uncertainties are used, while in the differential cross-sections no fit is performed.
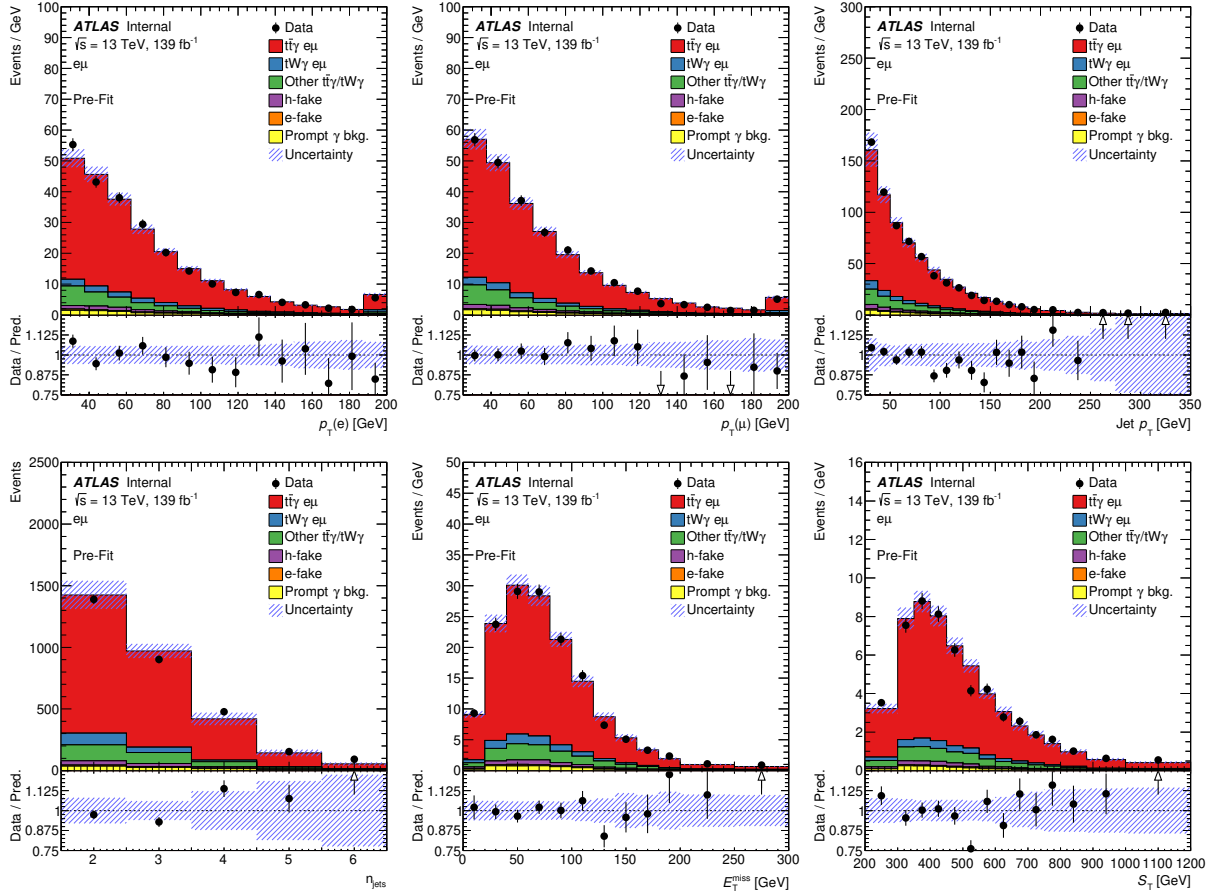
Not reviewed, for internal circulation only

Figure 1: Distributions of the transverse momentum of the electron, the muon and all jets (top row), and the number of jets, E_T^{miss} and S_T (bottom row) after event selection and before the likelihood fit. The combination of all $t\bar{t}\gamma$ and $tW\gamma$ categories is scaled to match the event yields in data. The shaded bands correspond to the statistical and systematic uncertainties (cf. Section 6) added in quadrature. Underflow and overflow events are included in the first and last bins of the distributions, respectively.

5.1 Fiducial region definition

The cross-sections are reported at parton level in a fiducial region, defined by the kinematic properties of the signal process, in which all selected final-state objects are produced within the detector acceptance. This is done in a way that mimics the event selection as defined in the theoretical calculation. Objects at parton level are taken from the MC simulation history. Photons and leptons are selected as stable particles after final state radiation. The leptons ($\ell = e, \mu$) must originate from W-boson decays and they are dressed with close-by photons within a cone of radius of $R = 0.1$ around them and must have $p_T > 25$ GeV and $|\eta| <$ 2.5. Only events with exactly one electron and one muon are considered. Events with leptons originating from an intermediate τ-lepton in the top-quark decay chain are not considered. The b-jets at parton level in the calculation from Refs. [10, 11] are jets clustered with the anti-k_t algorithm with a radius of $R = 0.4$. Since showering and hadronisation effects are not considered in this calculation, the jets correspond to the b-quarks from the top quark decay (with an additional parton in the cases where the NLO real emission leads to a parton close by a b-quark). To mimic this definition in the LO MC simulation, parton-level b-jets are defined as follows. The anti-k_t algorithm with a distance parameter $R = 0.4$ is applied to all partons

253 that are radiated from the two *b*-quarks (including the *b*-quarks themselves) and from the two initial partons.
254 The jets that include a *b*-quark from the decay of a top quark are selected as *b*-jets. The event is kept if
255 there are two *b*-jets satisfying $p_T > 25$ GeV and $|\eta| < 2.5$. Exactly one photon with $E_T > 20$ GeV and
256 $|\eta| < 2.37$ is required. Photons are required to be isolated from nearby jets by imposing a modified cone
257 approach as described in Ref. [56], as it is also done in Refs. [10, 11] to ensure soft and collinear safety.
258 The event is dropped if any of the following requirements is not fulfilled: $\Delta R(\gamma, \ell) > 0.4$, $\Delta R(e, \mu) > 0.4$,
259 $\Delta R(b, \bar{b}) > 0.4$ or $\Delta R(\ell, b) > 0.4$.

5.2 Fiducial inclusive cross-section

The fiducial inclusive cross-section is extracted using a profile likelihood fit to the S_T distribution. The
expected signal and background distributions are modelled in the fit using template distributions constructed
from the simulated samples. The parameter of interest, the fiducial cross-section σ_{fid}, is related to the
number of signal events in bin i of the S_T distribution as:

$$N_i^s = L \times \sigma_{\text{fid}} \times C \times f_i^{S_T}.$$

L is the integrated luminosity, $f_i^{S_T}$ is the fraction of generated signal events falling into bin i of the S_T
distribution after fiducial requirements are applied, and C is the correction factor for the signal efficiency ϵ
and for migration into the fiducial region f_{out}, defined as follows:

$$f_{\text{out}} = \frac{N_{\text{reco}}^{\text{non-fid}}}{N_{\text{reco}}}, \qquad \epsilon = \frac{N_{\text{reco}}^{\text{fid}}}{N_{\text{MC}}^{\text{fid}}} \qquad \Rightarrow C = \frac{\epsilon}{1 - f_{\text{out}}} = \frac{N_{\text{reco}}}{N_{\text{MC}}^{\text{fid}}},$$

261 where N_{reco} is the simulated number of signal events passing the event selection described in Section 4, and
262 $N_{\text{MC}}^{\text{fid}}$ is the corresponding number of signal events generated in the fiducial region defined in Section 5.1.
263 $N_{\text{reco}}^{\text{fid}}$ and $N_{\text{reco}}^{\text{non-fid}}$ are the number of signal events that pass the event selection and are generated within and
264 outside the fiducial region, respectively. The efficiency and outside migration are obtained from simulated
265 $t\bar{t}\gamma$ and $tW\gamma$ events. The correction factor is estimated from the signal simulation to be $C = 0.462$.

The likelihood function $\mathcal{L}$, based on Poisson statistics, is given by:

$$\mathcal{L} = \prod_i P(N_i^{\text{obs}} | N_i^s(\vec{\theta}) + \sum_b N_i^b(\vec{\theta})) \times \prod_t G(0 | \theta_t, 1).$$

266 N_i^{obs}, N_i^s, and N_i^b are the observed number of events in data, the predicted number of signal events, and the
267 estimated number of background events in bin i of the S_T distribution, respectively. Also the rates of those
268 $t\bar{t}\gamma$ and $tW\gamma$ events not counted as part of the signal and categorised as *Other* $t\bar{t}\gamma/tW\gamma$ are scaled with the
269 same parameter as the signal events in the fit, that is, no independent production cross-section is assumed
270 for these parts of the simulated $t\bar{t}\gamma/tW\gamma$ process. The term $\vec{\theta}$ represents the nuisance parameters that
271 describe the sources of systematic uncertainties. Each nuisance parameter θ_t is constrained by a Gaussian
272 distribution, $G(0 | \theta_t, 1)$. The width of the Gaussian corresponds to a change of ± 1 standard deviation of
273 the corresponding quantity in the likelihood. For systematic uncertainties related to the finite number of
274 simulated MC events, the Gaussian terms in the likelihood are replaced by Poisson terms. Each systematic
275 uncertainty affects N_i^s and N_i^b in each bin of the distribution. The cross-section is measured by profiling
276 the nuisance parameters and maximising this likelihood.

5.3 Normalised and absolute differential cross-sections

The measurements of the normalised and absolute differential cross-sections are performed as functions of the p_T and $|\eta|$ of the photon, and of angular variables between the photon and the leptons: ΔR between the photon and the closest lepton $\Delta R(\gamma, \ell)_{\min}$, as well as $\Delta\phi(\ell,\ell)$ and $|\Delta\eta(\ell,\ell)|$ between the two leptons. The kinematic properties of the photon are sensitive to the $t\gamma$ coupling. In particular, $\Delta R(\gamma, \ell)_{\min}$ is related to the angle between the top quark and the radiated photon which can give insight into the structure of this coupling. The distributions of $\Delta\phi(\ell,\ell)$ and $|\Delta\eta(\ell,\ell)|$ are sensitive to the $t\bar{t}$ spin correlation. The corresponding distributions in data compared to the SM simulations are shown in Figure 2.
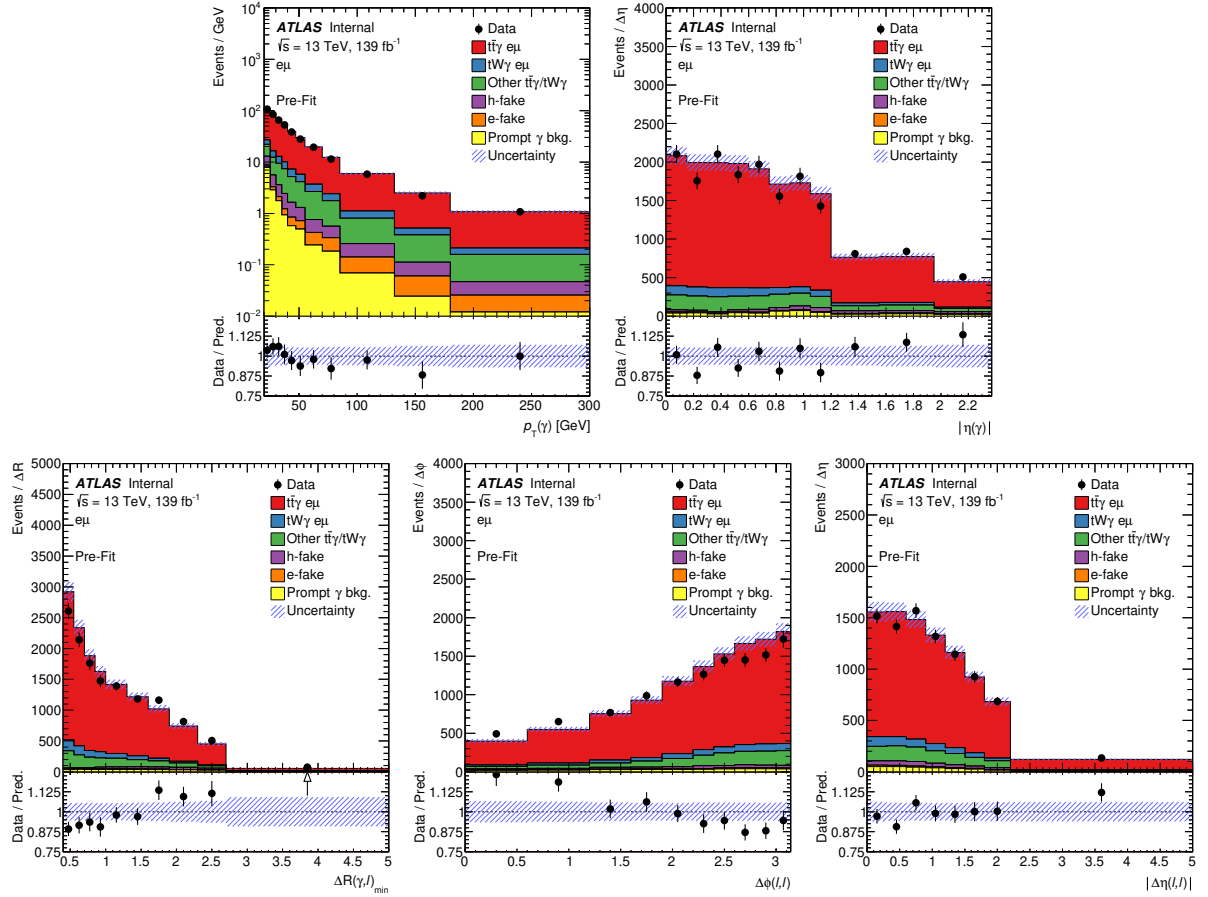
Figure 2: Distributions of the photon p_T and $|\eta|$ in the top row, and $\Delta R(\gamma, \ell)_{\min}$, $\Delta\phi(\ell,\ell)$ and $|\Delta\eta(\ell,\ell)|$ in the bottom row after event selection and before the likelihood fit. The combination of all $t\bar{t}\gamma$ and $tW\gamma$ categories is scaled to match the event yields in data. The shaded bands correspond to the statistical and systematic uncertainties (cf. Section 6) added in quadrature. Underflow and overflow events are included in the first and last bins of the distributions, respectively.

The data are corrected for detector resolution and acceptance effects to parton level in the fiducial phase space using an iterative Bayesian unfolding procedure [57] implemented in the RooUnfold package [58]. The differential cross-section is defined as:

$$\frac{d\sigma}{dX_k} = \frac{1}{L \times \Delta X_k \times \epsilon_k} \times \sum_j M_{jk}^{-1} \times (N_j^{\text{obs}} - N_j^b) \times f_{e\mu,j} \times (1 - f_{\text{out},j}) \,.$$

The indices j and k represent the bin indices of the observable X at detector and parton levels, respectively. The variable N_j^{obs} is the number of observed events, and N_j^b is the number of estimated non-$t\bar{t}\gamma/tW\gamma$ background events (pre-fit) in bin j at detector level. The contribution from the *Other $t\bar{t}\gamma/tW\gamma$* category is taken into account by correcting the remaining number of observed events by the signal fraction, $f_{e\mu,j}$, defined as the ratio of the number of selected $t\bar{t}\gamma$ and $tW\gamma$ $e\mu$ events to the total number of selected $t\bar{t}\gamma$ and $tW\gamma$ events, as determined from simulation. This avoids the dependence on the inclusive signal cross-section used for the normalisation. The efficiency ϵ_k is the fraction of signal events generated at parton level in bin k of the fiducial region, that are reconstructed and selected at detector level. L corresponds to the total integrated luminosity and ΔX_k represents the bin width. The migration matrix M_{kj} describes the detector response and expresses the probability for an event in bin k at parton level to be reconstructed in bin j at detector level, calculated from events passing both the fiducial-region selection and the event selection. The outside-migration fraction $f_{\text{out},j}$ is the fraction of signal events generated outside the fiducial region but reconstructed and selected in bin j at detector level. The normalised differential cross-section is derived by dividing the absolute result by the total cross-section, obtained by integrating over all bins of the observable.

The signal MC samples are used to determine ϵ_k, $f_{\text{out},j}$, and M_{kj}. The unfolding method relies on the Bayesian probability formula, starting from a given prior of the parton-level distribution and iteratively updating it with the posterior distribution. The binning choices of the unfolded observables take into account the detector resolution and the expected statistical uncertainty. The bin width has to be larger than twice the resolution, and the statistical uncertainty is required to be around or below 10% across all bins, with the latter being the dominant factor. The resolution of the lepton and photon momenta is very high and, therefore, the fraction of events migrating from one bin to another is extremely small. In all bins, the purity, defined as the fraction of reconstructed events that originate from the same bin, is larger than 80%, and it is above 90% for all observables except for the p_{T} of the photon. The number of iterations chosen is two, which provides good convergence of the unfolding distribution and a statistically stable result. For illustration purposes, the migration matrix, the efficiency, and the outside-migration fraction obtained for the distribution of the photon p_{T} are presented in Figure 3. The performance of the unfolding procedure is tested for possible biases from the choice of the input model. It has been verified that by reweighting the shape of the signal simulation by up to 50% with respect to the nominal shape, the unfolding procedure based on the nominal response matrix reproduces the altered shapes within the statistical uncertainties.

6 Systematic uncertainties

Different sources of systematic uncertainties are considered arising from detector effects, as well as theoretical uncertainties. Signal and background predictions are subject to these uncertainties.

6.1 Experimental uncertainties

Experimental systematic uncertainties affect the normalisation and shape of the distributions of the simulated signal and background samples. These include reconstruction and identification efficiency uncertainties, as well as uncertainties on the energy and momentum scale and resolution for the reconstructed physics objects in the analysis, including leptons, photons, jets and $E_{\text{T}}^{\text{miss}}$. In addition, uncertainties on flavour-tagging of jets, the jet vertex tagger (JVT) discriminant, the integrated luminosity value and the pile-up simulation are considered.
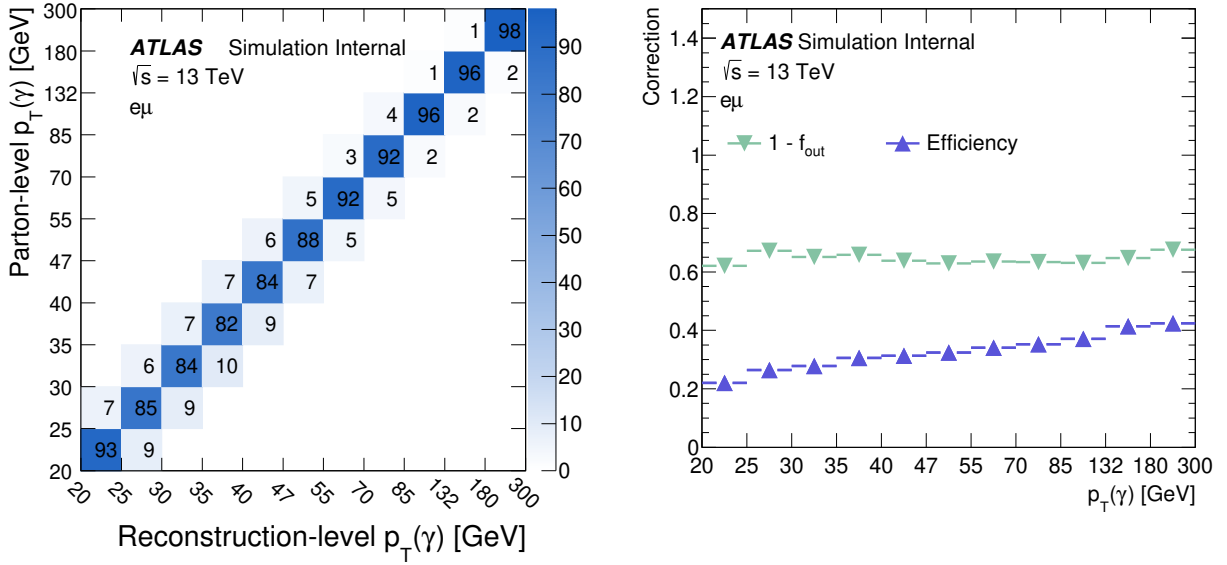
Figure 3: Left: migration matrix relating the photon p_T at the reconstruction and parton levels in the fiducial phase space, normalised by column and shown as percentages. Right: signal reconstruction and selection efficiency (ϵ) and $(1 - f_{out})$ fraction as a function of the photon p_T.

The photon identification and isolation efficiencies as well as the efficiencies of the lepton reconstruction, identification, isolation, and trigger in the MC samples are all corrected using scale factors to match the corresponding values in data. Similarly, corrections to the lepton and photon momentum scale and resolution are applied in simulation [45, 47]. All these corrections, which are p_T and η dependent, are varied within their uncertainties to study their impact on the final results.

The jet energy scale (JES) uncertainty is derived using a combination of simulations, test-beam data and *in-situ* measurements [51]. Additional contributions from jet-flavour composition, η-intercalibration, punch-through, single-particle response, calorimeter response to different jet flavours, and pile-up are taken into account, resulting in 29 uncorrelated JES uncertainty subcomponents. The most relevant JES uncertainties are related to the pile-up correction (*JES pile-up correction*) and modelling aspects of the in-situ calibration (*JES in-situ calibration*). The jet energy resolution (JER) in simulation is smeared by the measured JER uncertainty [59] split in 8 uncorrelated sources. The uncertainty associated with the JVT discriminant is obtained by varying the efficiency correction factors (labelled *jet vertex tagging* in the results, c.f. Figure 4).

The uncertainties related to the *b*-jet tagging calibration are determined separately for *b*-jets, *c*-jets and light-jets [60–62]. For each jet category, the uncertainties are decomposed into several uncorrelated components. The corrections are varied by their measured uncertainties.

The uncertainties associated with energy scales and resolutions of photons, leptons and jets are propagated to the E_T^{miss}. Additional uncertainties originate from the modelling of its soft term [63].

The uncertainty in the combined 2015–2018 integrated luminosity is 1.7% [64], obtained using the LUCID-2 detector [65] for the primary luminosity measurements.

The uncertainty associated to the modelling of pile-up in the simulation is assessed by varying the pile-up reweighting in the simulation within its uncertainties.

6.2 Signal and background modelling uncertainties

The $t\bar{t}\gamma$ signal modelling uncertainties include the uncertainties owing to the choice of the QCD scales, the parton shower, the amount of initial state radiation (ISR) and the PDF set. The QCD scale uncertainty is evaluated by varying the renormalisation and factorisation scales separately up and down by a factor of two from their nominal choices. The uncertainty on the parton shower and hadronisation ($t\bar{t}\gamma$ *PS model*) is estimated by comparing the $t\bar{t}\gamma$ nominal samples, produced with MADGRAPH5_aMC@NLO + PYTHIA 8, with an alternative sample interfaced to HERWIG 7. The ISR uncertainty ($t\bar{t}\gamma$ *ISR*) is studied by comparing the variations of the A14 tune parameter for radiation with its nominal values in the MADGRAPH5_aMC@NLO + PYTHIA 8 sample [24]. The PDF uncertainty ($t\bar{t}\gamma$ *PDF*) is evaluated using the standard deviation in each bin of the respective distribution formed by the set of 100 replicas of the NNPDF set [23].

For the $tW\gamma$ process the uncertainties on the renormalisation and factorisation scales are also estimated by varying them up and down separately by a factor of two with respect to the nominal sample value. A systematic uncertainty on the parton shower and hadronisation model is considered by comparing PYTHIA 8 and HERWIG 7 both interfaced to MADGRAPH5_aMC@NLO.

The used simulations of the $tW\gamma$ process are generated in the five-flavour scheme at leading order in QCD and the spectator b-quark is not included in the matrix-element generation step. The spectator b-quark expected to be produced in the initial state through the PDF, is only found in a fraction of the events at parton level in the MC simulation. The fractions of generated $tW\gamma$ events without spectator b-quark were found to be between 30% and 50% for the MC samples interfaced with HERWIG and PYTHIA, respectively. Therefore, an additional uncertainty associated to this possibly lost b-quark is assigned ($tW\gamma$ *parton definition*) as follows. With respect to the nominal $tW\gamma$ simulation, the parton-level event yields are doubled, assuming all b-jets are found, while the number of reconstructed events is kept constant. This leads to a variation of the correction factor C.

Several uncertainties of the modelling of $t\bar{t}$ processes, which give a dominant contribution to the h-fake and prompt γ background categories, are considered as shape-only uncertainties. The uncertainties on the parton shower and hadronisation are estimated by comparing the nominal simulation with alternative showering by HERWIG 7. Uncertainties in the modeling of ISR are estimated by evaluating variations of four different parameters in the POWHEG + PYTHIA 8 generator setup described in the following. Uncertainties on the renormalisation and factorisation scales are estimated by varying them up and down independently by a factor of two with respect to the default scale choice. These scale variations are implemented with corresponding weights which are available as part of the nominal MC sample. Uncertainties on the value of α_S used in the ISR parton shower modelling are estimated by comparing the nominal POWHEG + PYTHIA 8 simulation to reweighted samples where the weights correspond to higher and lower radiation parameter settings in the A14 tune, controlled by the *var3c* parameter in PYTHIA 8 which is varied by factors of 0.5 and 2.0. An additional ISR uncertainty is obtained by comparing the nominal sample with an additional one where the h_{damp} parameter, which controls the p_{T} of the first additional emission, is varied by a factor of 2.

In addition to those background modelling uncertainties, global normalisation uncertainties of 50% are assigned to the three categories h-fake photons, e-fake photons and prompt γ background [9] (*h-fakes*, *e-fakes*, and *prompt γ normalisation*).

6.3 Treatment of the systematic uncertainties in the measurements

As stated in Section 5, the impact of systematic uncertainties on the inclusive cross-section measurement is taken into account via nuisance parameters in the likelihood function. The nuisance parameters $\vec{\theta}$ are profiled in the maximum likelihood fit. Variations of the nuisance parameters can affect the shape as well as the rate of the S_T distribution. In case of signal modelling uncertainties, the rate uncertainty is composed of variations of the efficiency ϵ and the fraction f_out. All simulated samples used to evaluate signal modelling uncertainties are scaled to the same number of events in the fiducial phase space, $N_\mathrm{MC}^\mathrm{fid}$. The only uncertainty that is not included as nuisance parameter in the likelihood fit is the uncertainty on the $tW\gamma$ parton definition. This uncertainty does not affect the number of reconstructed events of the corresponding template in the likelihood fit. It only comprises an uncertainty on the number of generated events in the fiducial phase space. Thus, the $tW\gamma$ parton definition uncertainty is added in quadrature to the post-fit result of the likelihood fit.

To avoid high sensitivity to statistical fluctuations due to the limited number of events of the MC samples used in systematic variations, *smoothing* techniques are applied to the MC templates used to evaluate the signal and background modelling systematic uncertainties in the template fit. Additionally, the systematic uncertainties are symmetrised, taking the average of the up- and down-variation as the uncertainty. In the cases where both variations have the same sign or only one variation is available (e.g. the uncertainty on the parton shower and hadronisation signal modelling) the largest variation or the available one, respectively, is taken as both the up- and down-variations for the corresponding source. The ISR uncertainty suffers from statistical fluctuations in the available $t\bar{t}\gamma$ MC samples, therefore a more conservative approach is chosen for the symmetrisation. In this case, the largest of the two variations is taken bin by bin and mirrored around the nominal prediction.

In the case of the differential cross-section measurements, the pre-fit systematic variations are used for the study since the measurement is still dominated by statistical uncertainties. The same symmetrisation approach described for the inclusive cross-section is used for this measurement. Each systematic uncertainty is determined individually in each bin of the measurement by varying the corresponding efficiency, resolution, and model parameter within its uncertainty. For each variation, the measured differential cross-section is recalculated and the difference with respect to the nominal result per bin is taken as the systematic uncertainty. The overall uncertainty in the measurement is then derived by adding all contributions in quadrature, assuming the sources of systematic uncertainty to be fully uncorrelated.

Sources of systematic uncertainty related only to the background prediction are evaluated by shifting the nominal distribution of the corresponding background process by its associated uncertainty. For the experimental uncertainties, the input is varied by the corresponding shift, which typically affects both shape and normalisation of signal and background processes. The resulting distribution is unfolded and compared with the nominal unfolded distribution and the difference is assigned as uncertainty. The systematic uncertainties due to signal modelling are evaluated by varying the signal corrections, that is, the migration matrix M_{kj}, the efficiency ϵ_k and the fraction $f_{\mathrm{out},j}$, and calculating the difference of the resulting unfolded distributions with respect to the nominal results.

7 Inclusive cross-section measurement

The number of signal events is extracted using a profile likelihood fit to the S_T distribution and is translated into the signal cross-section in the fiducial phase space given by the kinematic boundaries of the signal as

Table 2: Illustrative summary of the systematic uncertainties grouped into different categories and their relative impact on the measurement of the inclusive fiducial cross-section (symmetrised). The categories "$t\bar{t}\gamma/tW\gamma$ modelling" and "Background modelling" include all corresponding systematic uncertainties described in Section 6.2. The "$tW\gamma$ parton definition" uncertainty is listed separately since it does not enter the likelihood fit directly as described in Section 6.3. The category "Photons" corresponds to the uncertainties related to photon identification and isolation. "Jets" includes the total uncertainty on JES, JER and JVT discriminant, while the b-tagging related uncertainties are given in a separate category ("Flavour-tagging"). The category "Leptons" represents the uncertainties related to lepton identification, isolation and energy/momentum calibration.

Category	Uncertainty
$t\bar{t}\gamma/tW\gamma$ modelling	3.8%
Background modelling	2.1%
Photons	1.9%
Luminosity	1.8%
Jets	1.6%
Pile-up	1.3%
Leptons	1.1%
Flavour-tagging	1.1%
MC statistics	0.4%
Soft term E_T^{miss}	0.2%
$tW\gamma$ parton definition	2.8%
Total syst.	6.3%

430 described in Section 5.

431 The best-fit values of the parameters ranked highest in impact and their impact on the result are shown
432 in Figure 4. The best fit values of the nuisance parameters correspond to variations that for most of the
433 parameters are within one standard deviation of the prior uncertainties. Rate and shape uncertainties on the
434 $t\bar{t}\gamma$ PS model and $t\bar{t}\gamma$ ISR variations are treated as separate nuisance parameters. This approach prevents
435 constraints on the rate uncertainty owing to differences in the shape of the S_T distribution between the data
436 and simulation, in particular in the tail where the data overshoot the prediction and the fit compensates for
437 this discrepancy by pulling the nuisance parameter of the $t\bar{t}\gamma$ PS model shape uncertainty. The impact of
438 the individual nuisance parameters is evaluated as the difference between the reference best-fit value of the
439 cross section and the one obtained when fixing the corresponding nuisance parameter under scrutiny to its
440 best-fit value and its ± one standard deviation. Table 2 shows the systematic uncertainties and their relative
441 impact on the measurement of the inclusive cross-section. The effect of each category of uncertainties is
442 calculated from the quadratic difference between the total uncertainty in the measured fiducial cross-section
443 and the uncertainty from the fit with the corresponding nuisance parameters fixed to their fitted values.
444 The uncertainties on the signal modelling, especially the rate uncertainties from the $t\bar{t}\gamma$ showering and the
445 ISR variation, have the largest impact on the result.

446 The distribution of the fitted S_T variable is shown in Figure 5. The dashed band represents the post-fit
447 uncertainties. The expected yields after the fit describe the data well.

448 Extrapolated to the fiducial phase space using the correction factor C, the fit result corresponds to an inclusive
449 cross-section for the combined $t\bar{t}\gamma/tW\gamma$ process in the $e\mu$ channel of $\sigma_{fid} = 39.6 \pm 0.8$ (stat) $^{+2.6}_{-2.2}$ (syst) fb =
450 $39.6\,^{+2.7}_{-2.3}$ fb. The measured cross-section is in good agreement with the dedicated theoretical calculation
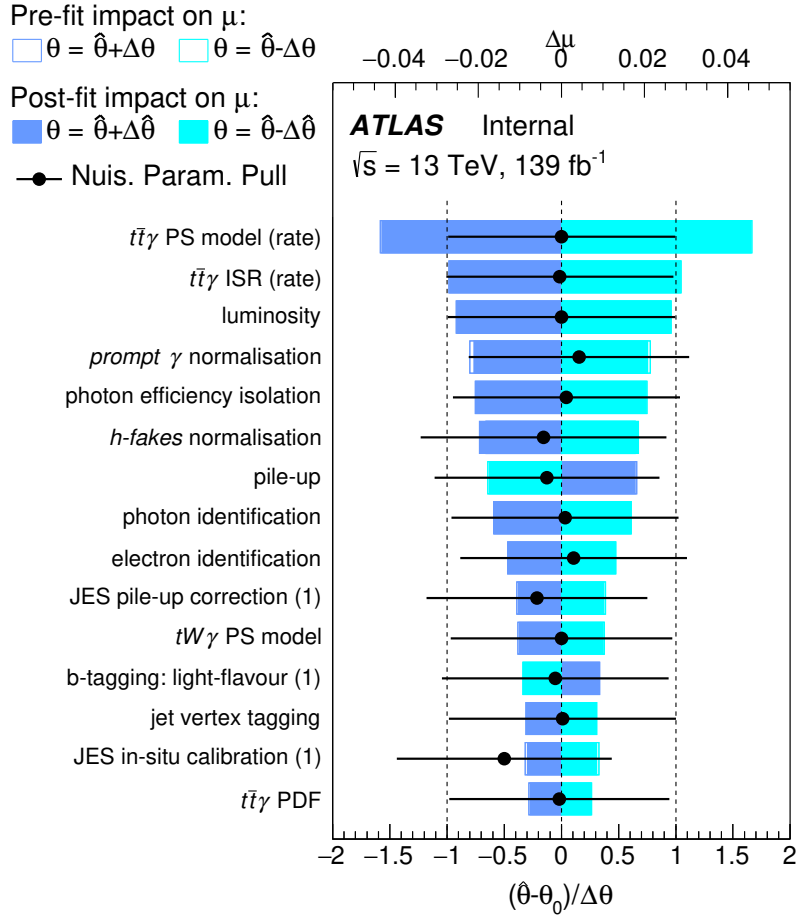
Figure 4: Ranking of the systematic uncertainties included in the maximum likelihood fit used in the inclusive cross-section measurement. The blue and turquoise bands indicate the post-fit impact on the fit result, whereas the outlined blue and turquoise rectangles show the pre-fit impact. The difference between the two reflects the constraint of the nuisance parameter due to correlations in the fit. The impact is overlaid with the post-fit values of the nuisance parameters (pulls) shown by the black dots. The black lines represent the post-fit uncertainties normalised to the pre-fit uncertainties.
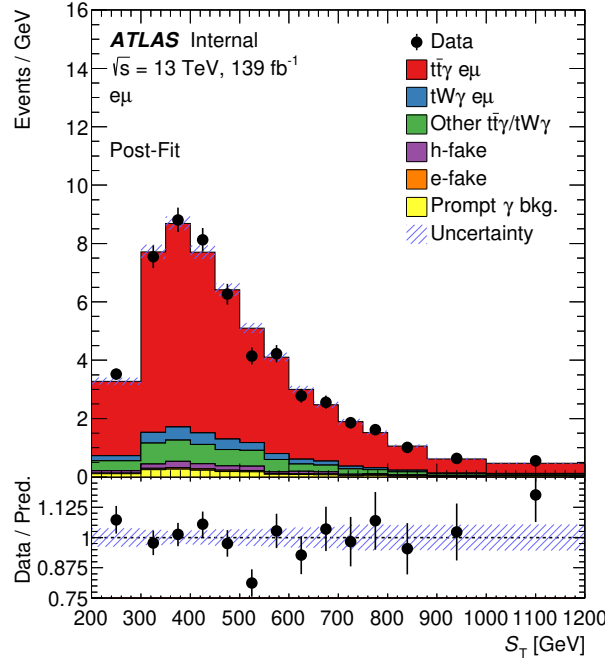
Figure 5: Post-fit distribution of the S_T variable. The uncertainty band represents the post-fit uncertainties. Underflow and overflow events are included in the first and last bins of the distribution, respectively.

provided by the authors of Refs. [10, 11], which predicts a value of $\sigma_{\text{fid}} = 38.50 \, {}^{+0.56}_{-2.18} \, (\text{scale}) \, {}^{+1.04}_{-1.18} \, (\text{PDF})$ fb for the chosen fiducial phase space using the CT14 PDF set [66]. The uncertainty on the theory prediction includes uncertainties owing to the scales and PDF. The PDF uncertainty is rescaled to the 68% CL. In the theoretical calculation, the renormalisation and factorisation scales are chosen as $H_T/4$, where H_T is the total transverse momentum of the system, defined as the scalar sum of the p_T of the leptons, b-jets, photon and the total missing p_T from the neutrinos. The mass of the top quark is set to 173.2 GeV. The electroweak coupling in the calculation is derived from the Fermi constant G_μ and it is set to $\alpha_{G_\mu} \approx 1/132$, while it is 1/137 for the leading emission. Further details can be found in Ref. [10].

8 Differential cross-section measurements

The normalised differential cross-sections are shown in Figure 6 while the absolute measured differential cross-sections are presented in Figure 7. The cross-sections are compared to the NLO calculation in the same fiducial phase space and to the combination of the $t\bar{t}\gamma$ and $tW\gamma$ LO MadGraph5_aMC@NLO simulations interfaced with Pythia 8 and Herwig 7, referred to as MG5_aMC+Pythia8 and MG5_aMC+Herwig7 in the following plots and tables. The shape of the measured differential distributions is generally well described by both, the LO MC predictions from MadGraph5_aMC@NLO as well as the NLO theory prediction. The latter tends to describe the shape of the measured distribution slightly better. The shape of the $\Delta\phi(\ell, \ell)$ is not perfectly modelled by the MadGraph5_aMC@NLO simulation, while the NLO prediction provides a better description of this distribution. The calculated χ^2/ndf values for the normalised and absolute cross-section and their corresponding p-values are summarised in Tables 3 and 4, quantifying

Table 3: χ^2/ndf and p-values between the measured normalised cross-sections and various predictions from the MC simulation and the NLO calculation.

Predictions	$p_T(\gamma)$		$|\eta(\gamma)|$		$\Delta R(\gamma, \ell)_{\text{min}}$		$\Delta\phi(\ell, \ell)$		$|\Delta\eta(\ell, \ell)|$	
	χ^2/ndf	p-value	χ^2/ndf	p-value	χ^2/ndf	p-value	χ^2/ndf	p-value	χ^2/ndf	p-value
$t\bar{t}\gamma + tW\gamma$ (MG5_aMC+Pythia8)	6.3/10	0.79	16.4/10	0.09	20.1/9	0.02	30.8/9	<0.01	6.5/7	0.48
$t\bar{t}\gamma + tW\gamma$ (MG5_aMC+Herwig7)	5.3/10	0.87	18.3/10	0.05	18.9/9	0.03	31.6/9	<0.01	6.8/7	0.45
Theory NLO	6.0/10	0.82	14.6/10	0.15	13.5/9	0.14	5.8/9	0.76	5.6/7	0.59

Table 4: χ^2/ndf and p-values between the measured absolute cross-sections and the NLO calculation.

Predictions	$p_T(\gamma)$		$|\eta(\gamma)|$		$\Delta R(\gamma, \ell)_{\text{min}}$		$\Delta\phi(\ell, \ell)$		$|\Delta\eta(\ell, \ell)|$	
	χ^2/ndf	p-value	χ^2/ndf	p-value	χ^2/ndf	p-value	χ^2/ndf	p-value	χ^2/ndf	p-value
Theory NLO	6.1/11	0.87	13.9/11	0.24	11.7/10	0.31	5.8/10	0.83	6.2/8	0.62

the compatibility between data and each of the predictions. The χ^2 values are calculated as:

$$\chi^2 = \sum_{j,k} (\sigma_{j,\text{data}} - \sigma_{j,\text{pred.}}) \cdot C_{jk}^{-1} \cdot (\sigma_{k,\text{data}} - \sigma_{k,\text{pred.}}),$$

where σ_{data} and $\sigma_{\text{pred.}}$ are the unfolded and predicted differential cross-sections, C_{jk} is the covariance matrix of σ_{data}, calculated as the sum of the covariance matrix for the statistical uncertainty and the covariance matrices for each of the systematic uncertainties, and j and k are the binning indices of the distribution. The covariance matrix for each of the systematic uncertainties is estimated as $\sigma_j \times \sigma_k$, where σ_j and σ_k are the symmetrised uncertainties for bin j and bin k of the unfolded distribution. In the case of the normalised differential cross-sections, the last bin is removed from the χ^2 calculation and the number of degrees of freedom is reduced by one.

The systematic uncertainties of the unfolded distributions are decomposed into signal modelling uncertainties, experimental uncertainties, and background modelling uncertainties. The breakdown of the categories of systematic uncertainties and the statistical one, which is the dominant source of uncertainty, are illustrated in Figures 8 and 9 for the normalised and absolute differential cross-sections, respectively. The systematic uncertainty is dominated by the background and signal modelling.

9 Conclusions

Measurements of the inclusive fiducial, as well as absolute and normalised differential production cross-sections of the combined $t\bar{t}\gamma/tW\gamma$ process in the $e\mu$ decay channel are presented using pp collisions at a centre-of-mass energy of 13 TeV, corresponding to an integrated luminosity of 139 fb^{-1}. For the estimation of efficiencies and acceptance corrections, a LO Monte Carlo simulation of the $2 \rightarrow 7$ process $pp \rightarrow e\nu\mu\nu bb\gamma$ was used for the $t\bar{t}\gamma$ part of the signal. The contribution from $tW\gamma$ was estimated from a combination of LO Monte Carlo simulations for the $2 \rightarrow 3$ process $pp \rightarrow tW\gamma$ and the $2 \rightarrow 6$ process $pp \rightarrow e\nu\mu\nu b\gamma$. The simulations include initial and final state radiation of the photon from all involved objects in the matrix element. The resonant top-quark production is taken into account in the simulation of $t\bar{t}\gamma$. Possible singly-resonant production leading to the same final state is included in the simulation of the $tW\gamma$ process.
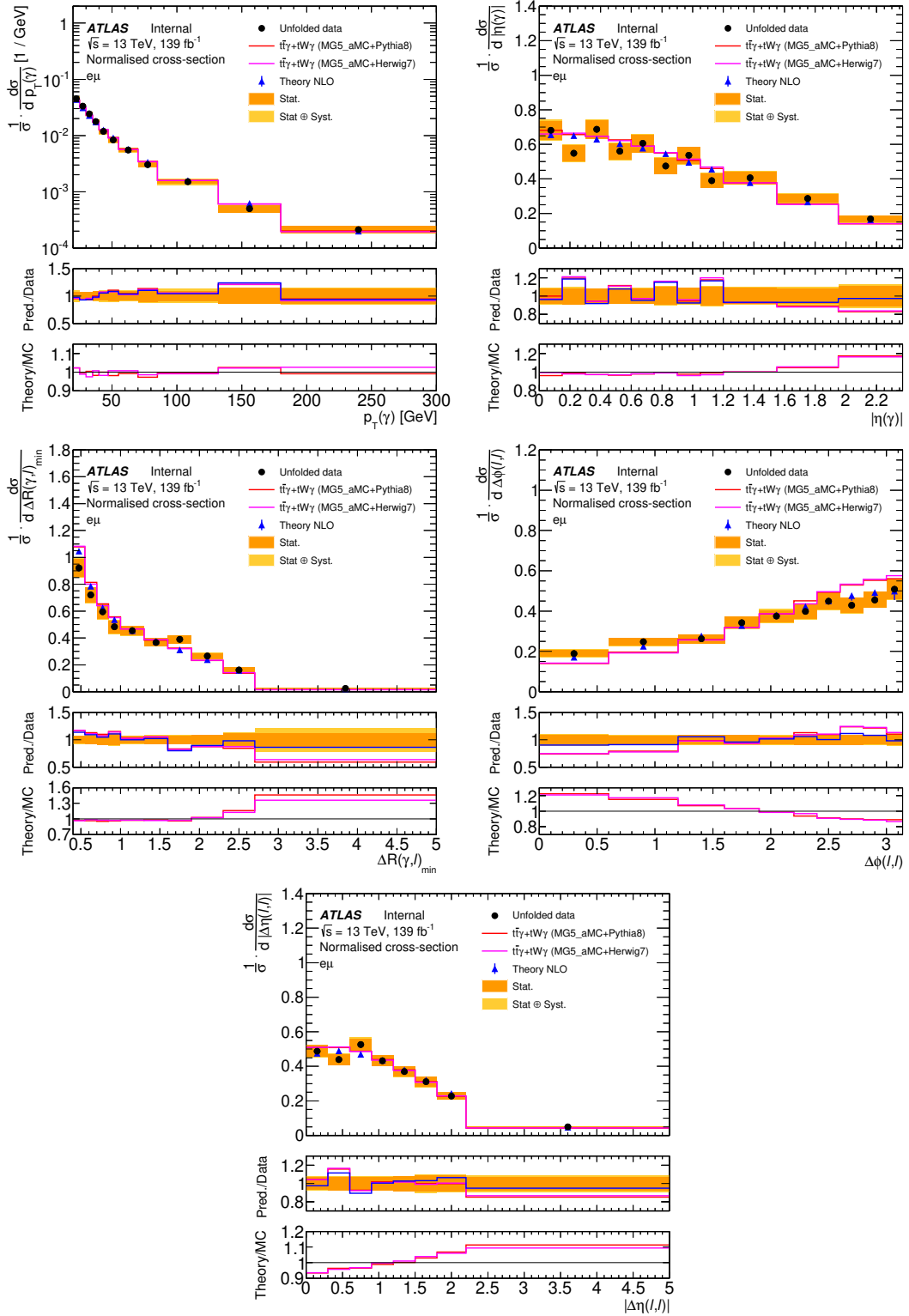
Not reviewed, for internal circulation only

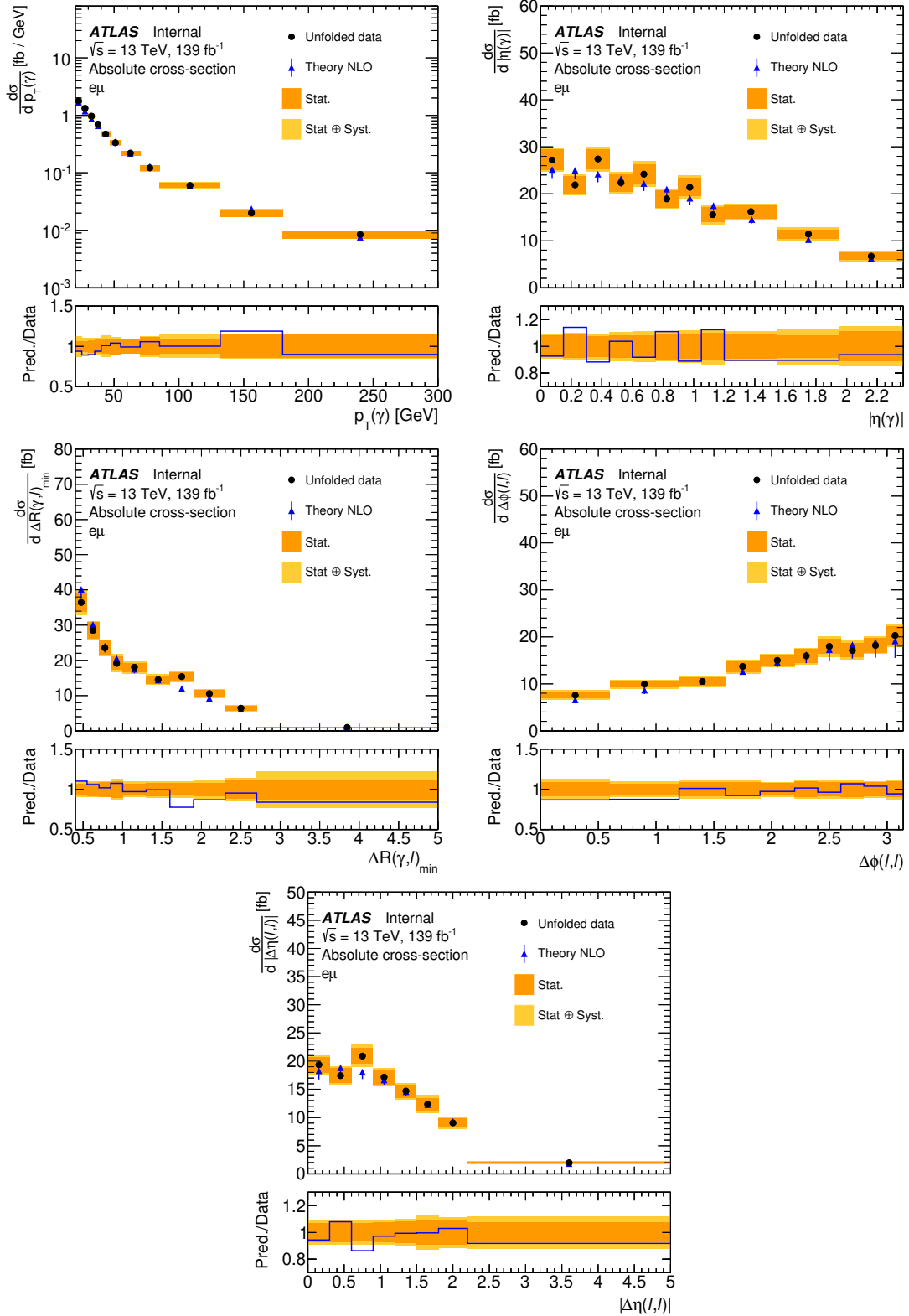Figure 6: Normalised differential cross-section measured in the fiducial phase space as a function of the photon p_T, photon $|\eta|$, $\Delta R(\gamma, \ell)_{min}$, $\Delta\phi(\ell, \ell)$, and $|\Delta\eta(\ell, \ell)|$ 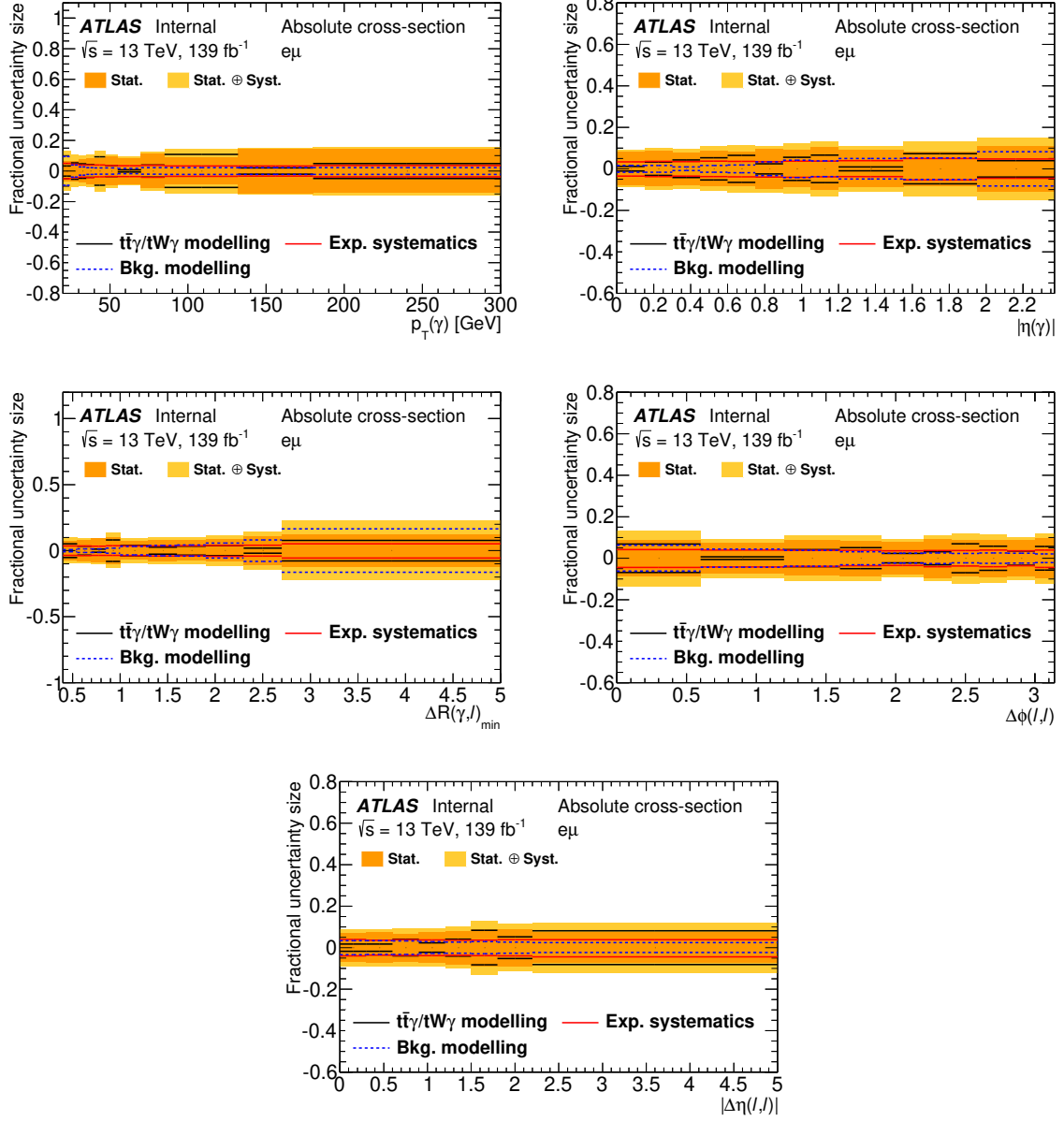(from left to right and top to bottom). Data are compared to the NLO calculation provided by the authors of Refs. [10, 11] and the MADGRAPH5_aMC@NLO simulation interfaced with PYTHIA 8 and HERWIG 7. The uncertainty on the calculation corresponds to the total scale and PDF uncertainties. The PDF uncertainty is rescaled to the 68% CL. The lower parts of each plot show the ratio of the prediction to the data and the ratio of the NLO calculation to the MC simulations.

Figure 7: Absolute differential cross-section measured in the fiducial phase space as a function of the photon p_T, photon $|\eta|$, $\Delta R(\gamma, \ell)_{\min}$, $\Delta\phi(\ell, \ell)$, and $|\Delta\eta(\ell, \ell)|$ (from left to right and top to bottom). Data are compared to the NLO calculation provided by the authors of Refs. [10, 11]. The uncertainty on the calculation corresponds to the total scale and PDF uncertainties. The PDF uncertainty is rescaled to the 68% CL. The lower part of each plot shows the ratio of the prediction to the data.

Not reviewed, for internal circulation only
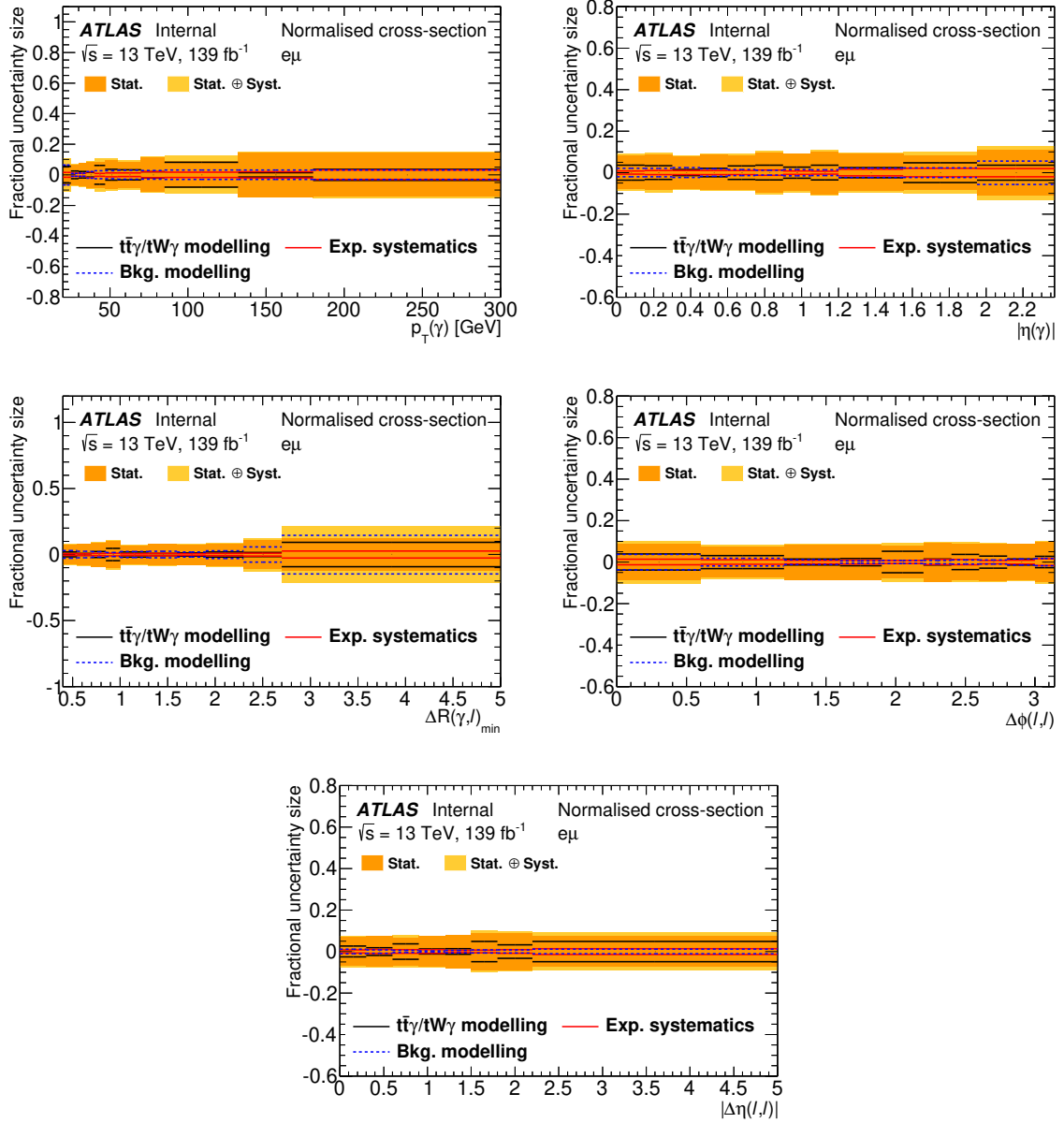
Figure 8: Contribution of each category of systematic uncertainties in each bin of the measurement of the normalised cross-sections as functions of the photon p_{T}, photon $|\eta|$, $\Delta R(\gamma, \ell)_{\mathrm{min}}$, $\Delta\phi(\ell, \ell)$ and $|\Delta\eta(\ell, \ell)|$ (from left to right and top to bottom).

Figure 9: Contribution of each category of systematic uncertainties in each bin of the measurement of the absolute cross-sections as functions of the photon p_T, photon $|\eta|$, $\Delta R(\gamma, \ell)_{min}$, $\Delta\phi(\ell, \ell)$ and $|\Delta\eta(\ell, \ell)|$.

The results are compared to the prediction from the LO Monte Carlo simulations and the dedicated NLO theory prediction provided by the authors of Refs. [10, 11], which includes all off-shell contributions. The measured inclusive cross-section of $\sigma = 39.6\,^{+2.7}_{-2.3}$ fb is found to be in good agreement with the predicted NLO cross-section. All considered differential distributions are also found to be well described by the theory.

Acknowledgements

References

[1] U. Baur, A. Juste, L. H. Orr and D. Rainwater, *Probing electroweak top quark couplings at hadron colliders*, Phys. Rev. **D71** (2005) 054013, arXiv: hep-ph/0412021 [hep-ph] (cit. on p. 2).

[2] A. O. Bouzas and F. Larios, *Electromagnetic dipole moments of the top quark*, Phys. Rev. **D87** (2013) 074015, arXiv: 1212.6575 [hep-ph] (cit. on p. 2).

[3] M. Schulze and Y. Soreq, *Pinning down electroweak dipole operators of the top quark*, Eur. Phys. J. **C76** (2016) 466, arXiv: 1603.08911 [hep-ph] (cit. on p. 2).

[4]   O. Bessidskaia Bylund, F. Maltoni, I. Tsinikos, E. Vryonidou and C. Zhang, *Probing top quark neutral couplings in the Standard Model Effective Field Theory at NLO in QCD*, JHEP **05** (2016) 052, arXiv: 1601.08193 [hep-ph] (cit. on p. 2).

[5]   CDF Collaboration (Aaltonen, T. et al.), *Evidence for $t\bar{t}\gamma$ production and measurement of $\sigma_{t\bar{t}\gamma}/\sigma_{t\bar{t}}$*, Phys. Rev. **D84** (2011) 031104, arXiv: 1106.3970 [hep-ex] (cit. on p. 2).

[6]   ATLAS Collaboration, *Observation of top-quark pair production in association with a photon and measurement of the $t\bar{t}\gamma$ production cross section in pp collisions at $\sqrt{s}$ = 7 TeV using the ATLAS detector*, Phys. Rev. D **91** (2015) 072007, arXiv: 1502.00586 [hep-ex] (cit. on p. 2).

[7]   ATLAS Collaboration, *Measurement of the $t\bar{t}\gamma$ production cross section in proton–proton collisions at $\sqrt{s}$ = 8 TeV with the ATLAS detector*, JHEP **11** (2017) 086, arXiv: 1706.03046 [hep-ex] (cit. on p. 2).

[8]   CMS Collaboration, *Measurement of the semileptonic $t\bar{t}+\gamma$ production cross section in pp collisions at $\sqrt{s}$ = 8 TeV*, JHEP **10** (2017) 006, arXiv: 1706.08128 [hep-ex] (cit. on p. 2).

[9]   ATLAS Collaboration, *Measurements of inclusive and differential fiducial cross-sections of $t\bar{t}\gamma$ production in leptonic final states at $\sqrt{s}$ = 13 TeV in ATLAS*, Eur. Phys. J. C **79** (2019) 382, arXiv: 1812.01697 [hep-ex] (cit. on pp. 2, 5, 13).

[10] G. Bevilacqua, H. B. Hartanto, M. Kraus, T. Weber and M. Worek, *Hard photons in hadroproduction of top quarks with realistic final states*, JHEP **10** (2018) 158, arXiv: 1803.09916 [hep-ph] (cit. on pp. 2, 4, 5, 8, 9, 17, 19, 20, 23).

[11] G. Bevilacqua, H. Hartanto, M. Kraus, T. Weber and M. Worek, *Precise predictions for $t\bar{t}\gamma/t\bar{t}$ cross section ratios at the LHC*, JHEP **01** (2019) 188, arXiv: 1809.08562 [hep-ph] (cit. on pp. 2, 4, 5, 8, 9, 17, 19, 20, 23).

[12] ATLAS Collaboration, *The ATLAS Experiment at the CERN Large Hadron Collider*, JINST **3** (2008) S08003 (cit. on p. 3).

[13] ATLAS Collaboration, *ATLAS Insertable B-Layer Technical Design Report*, ATLAS-TDR-19, 2010, URL: https://cds.cern.ch/record/1291633, *ATLAS Insertable B-Layer Technical Design Report Addendum*, ATLAS-TDR-19-ADD-1, 2012, URL: https://cds.cern.ch/record/1451888 (cit. on p. 3).

[14] B. Abbott et al., *Production and integration of the ATLAS Insertable B-Layer*, JINST **13** (2018) T05008, arXiv: 1803.00844 [physics.ins-det] (cit. on p. 3).

[15] ATLAS Collaboration, *Performance of the ATLAS trigger system in 2015*, Eur. Phys. J. C **77** (2017) 317, arXiv: 1611.09661 [hep-ex] (cit. on p. 3).

[16] ATLAS Collaboration, *The ATLAS Simulation Infrastructure*, Eur. Phys. J. C **70** (2010) 823, arXiv: 1005.4568 [physics.ins-det] (cit. on p. 3).

[17] S. Agostinelli et al., *Geant4 – a simulation toolkit*, Nucl. Instrum. Meth. A **506** (2003) 250 (cit. on p. 3).

[18] T. Sjöstrand, S. Mrenna and P. Skands, *PYTHIA 6.4 physics and manual*, JHEP **05** (2006) 026, arXiv: hep-ph/0603175 (cit. on p. 3).

[19] T. Sjöstrand et al., *An introduction to PYTHIA 8.2*, Comput. Phys. Commun. **191** (2015) 159, arXiv: 1410.3012 [hep-ph] (cit. on p. 3).

[20] ATLAS Collaboration, *Summary of ATLAS Pythia 8 tunes*, ATL-PHYS-PUB-2012-003, 2012, URL: https://cds.cern.ch/record/1474107 (cit. on p. 3).

[21] A. D. Martin, W. J. Stirling, R. S. Thorne and G. Watt, *Parton distributions for the LHC*, Eur. Phys. J. C**63** (2009) 189, arXiv: `0901.0002 [hep-ph]` (cit. on p. 3).

[22] J. Alwall et al., *The automated computation of tree-level and next-to-leading order differential cross sections, and their matching to parton shower simulations*, JHEP **07** (2014) 079, arXiv: `1405.0301 [hep-ph]` (cit. on p. 3).

[23] J. Pumplin et al., *New Generation of Parton Distributions with Uncertainties from Global QCD Analysis*, JHEP **07** (2002) 012, arXiv: `hep-ph/0201195` (cit. on pp. 3, 13).

[24] ATLAS Collaboration, *ATLAS Pythia 8 tunes to 7 TeV data*, ATL-PHYS-PUB-2014-021, 2014, URL: `https://cds.cern.ch/record/1966419` (cit. on pp. 4, 13).

[25] D. J. Lange, *The EvtGen particle decay simulation package*, Nucl. Instrum. Meth. A **462** (2001) 152 (cit. on p. 4).

[26] T. Gleisberg et al., *Event generation with SHERPA 1.1*, JHEP **02** (2009) 007, arXiv: `0811.4622 [hep-ph]` (cit. on p. 4).

[27] S. Höche, F. Krauss, S. Schumann and F. Siegert, *QCD matrix elements and truncated showers*, JHEP **05** (2009) 053, arXiv: `0903.1219 [hep-ph]` (cit. on p. 4).

[28] T. Gleisberg and S. Höche, *Comix, a new matrix element generator*, JHEP **12** (2008) 039, arXiv: `0808.3674 [hep-ph]` (cit. on p. 4).

[29] S. Schumann and F. Krauss, *A parton shower algorithm based on Catani–Seymour dipole factorisation*, JHEP **03** (2008) 038, arXiv: `0709.1027 [hep-ph]` (cit. on p. 4).

[30] S. Höche, F. Krauss, M. Schönherr and F. Siegert, *A critical appraisal of NLO+PS matching methods*, JHEP **09** (2012) 049, arXiv: `1111.1220 [hep-ph]` (cit. on p. 4).

[31] S. Catani, F. Krauss, B. R. Webber and R. Kuhn, *QCD matrix elements + parton showers*, JHEP **11** (2001) 063, arXiv: `hep-ph/0109231 [hep-ph]` (cit. on p. 4).

[32] S. Höche, F. Krauss, M. Schönherr and F. Siegert, *QCD matrix elements + parton showers. The NLO case*, JHEP **04** (2013) 027, arXiv: `1207.5030 [hep-ph]` (cit. on p. 4).

[33] F. Cascioli, P. Maierhöfer and S. Pozzorini, *Scattering Amplitudes with Open Loops*, Phys. Rev. Lett. **108** (2012) 111601, arXiv: `1111.5206 [hep-ph]` (cit. on p. 4).

[34] A. Denner, S. Dittmaier and L. Hofer, *COLLIER: A fortran-based complex one-loop library in extended regularizations*, Comput. Phys. Commun. **212** (2017) 220, arXiv: `1604.06792 [hep-ph]` (cit. on p. 4).

[35] P. Nason, *A new method for combining NLO QCD with shower Monte Carlo algorithms*, JHEP **11** (2004) 040, arXiv: `hep-ph/0409146` (cit. on p. 4).

[36] S. Frixione, P. Nason and C. Oleari, *Matching NLO QCD computations with parton shower simulations: the POWHEG method*, JHEP **11** (2007) 070, arXiv: `0709.2092 [hep-ph]` (cit. on p. 4).

[37] S. Alioli, P. Nason, C. Oleari and E. Re, *A general framework for implementing NLO calculations in shower Monte Carlo programs: the POWHEG BOX*, JHEP **06** (2010) 043, arXiv: `1002.2581 [hep-ph]` (cit. on p. 4).

[38] R. D. Ball et al., *Parton distributions for the LHC Run II*, JHEP **04** (2015) 040, arXiv: `1410.8849 [hep-ph]` (cit. on p. 4).

[39] M. Czakon and A. Mitov, *Top++: A program for the calculation of the top-pair cross-section at hadron colliders*, Comput. Phys. Commun. **185** (2014) 2930, arXiv: 1112.5675 [hep-ph] (cit. on p. 4).

[40] ATLAS Collaboration, *Measurement of $W^{\pm}$ and Z-boson production cross sections in pp collisions at $\sqrt{s}$ = 13 TeV with the ATLAS detector*, Phys. Lett. B **759** (2016) 601, arXiv: 1603.09222 [hep-ex] (cit. on p. 4).

[41] J. M. Campbell and R. K. Ellis, *Update on vector boson pair production at hadron colliders*, Phys. Rev. D **60** (1999) 113006, arXiv: hep-ph/9905386 (cit. on p. 4).

[42] D. de Florian et al., *Handbook of LHC Higgs cross sections: 4. Deciphering the nature of the Higgs sector*, (2016), arXiv: 1610.07922 [hep-ph] (cit. on p. 5).

[43] ATLAS Collaboration, *Performance of electron and photon triggers in ATLAS during LHC Run 2*, (2019), arXiv: 1909.00761 [hep-ex] (cit. on p. 5).

[44] ATLAS Collaboration, *Electron and photon performance measurements with the ATLAS detector using the 2015-2017 LHC proton–proton collision data*, (2019), arXiv: 1908.00005 [hep-ex] (cit. on pp. 5, 6).

[45] ATLAS Collaboration, *Muon reconstruction performance of the ATLAS detector in proton–proton collision data at $\sqrt{s}$ = 13 TeV*, Eur. Phys. J. C **76** (2016) 292, arXiv: 1603.05598 [hep-ex] (cit. on pp. 6, 12).

[46] ATLAS Collaboration, *Measurement of the photon identification efficiencies with the ATLAS detector using LHC Run 2 data collected in 2015 and 2016*, Eur. Phys. J. C **79** (2019) 205, arXiv: 1810.05087 [hep-ex] (cit. on p. 6).

[47] ATLAS Collaboration, *Electron and photon energy calibration with the ATLAS detector using 2015–2016 LHC proton–proton collision data*, JINST **14** (2019) P03017, arXiv: 1812.03848 [hep-ex] (cit. on pp. 6, 12).

[48] M. Cacciari, G. P. Salam and G. Soyez, *The anti-k_t jet clustering algorithm*, JHEP **04** (2008) 063, arXiv: 0802.1189 [hep-ph] (cit. on p. 6).

[49] M. Cacciari, G. P. Salam and G. Soyez, *FastJet user manual*, Eur. Phys. J. C **72** (2012) 1896, arXiv: 1111.6097 [hep-ph] (cit. on p. 6).

[50] ATLAS Collaboration, *Properties of jets and inputs to jet reconstruction and calibration with the ATLAS detector using proton–proton collisions at $\sqrt{s}$ = 13 TeV*, ATL-PHYS-PUB-2015-036, 2015, URL: https://cds.cern.ch/record/2044564 (cit. on p. 6).

[51] ATLAS Collaboration, *Jet energy scale measurements and their systematic uncertainties in proton–proton collisions at $\sqrt{s}$ = 13 TeV with the ATLAS detector*, Phys. Rev. D **96** (2017) 072002, arXiv: 1703.09665 [hep-ex] (cit. on pp. 6, 12).

[52] ATLAS Collaboration, *Tagging and suppression of pileup jets with the ATLAS detector*, ATLAS-CONF-2014-018, 2014, URL: https://cds.cern.ch/record/1700870 (cit. on p. 6).

[53] ATLAS Collaboration, *Optimisation and performance studies of the ATLAS b-tagging algorithms for the 2017-18 LHC run*, ATL-PHYS-PUB-2017-013, 2017, URL: https://cds.cern.ch/record/2273281 (cit. on p. 6).

[54] ATLAS Collaboration, *Measurements of b-jet tagging efficiency with the ATLAS detector using $t\bar{t}$ events at $\sqrt{s}$ = 13 TeV*, JHEP **08** (2018) 089, arXiv: 1805.01845 [hep-ex] (cit. on p. 6).

[55] ATLAS Collaboration, E_T^{miss} *performance in the ATLAS detector using 2015–2016 LHC pp collisions*, ATLAS-CONF-2018-023, 2018, URL: https://cds.cern.ch/record/2625233 (cit. on p. 6).

[56] S. Frixione, *Isolated photons in perturbative QCD*, Phys. Lett. **B429** (1998) 369, arXiv: hep-ph/9801442 [hep-ph] (cit. on p. 9).

[57] G. D'Agostini, *A multidimensional unfolding method based on Bayes' theorem*, Nucl. Instrum. Meth. A **362** (1995) 487 (cit. on p. 10).

[58] T. Adye, *Unfolding algorithms and tests using RooUnfold*, 2011, arXiv: 1105.1160 [physics.data-an] (cit. on p. 10).

[59] ATLAS Collaboration, *Jet Calibration and Systematic Uncertainties for Jets Reconstructed in the ATLAS Detector at* $\sqrt{s}$ = 13 *TeV*, ATL-PHYS-PUB-2015-015, 2015, URL: https://cds.cern.ch/record/2037613 (cit. on p. 12).

[60] ATLAS Collaboration, *Measurements of b-jet tagging efficiency with the ATLAS detector using* $t\bar{t}$ *events at* $\sqrt{s}$ = 13 *TeV*, JHEP **08** (2018) 089, arXiv: 1805.01845 [hep-ex] (cit. on p. 12).

[61] ATLAS Collaboration, *Measurement of b-tagging efficiency of c-jets in* $t\bar{t}$ *events using a likelihood approach with the ATLAS detector*, ATLAS-CONF-2018-001, 2018, URL: https://cds.cern.ch/record/2306649 (cit. on p. 12).

[62] ATLAS Collaboration, *Calibration of light-flavour b-jet mistagging rates using ATLAS proton–proton collision data at* $\sqrt{s}$ = 13 *TeV*, ATLAS-CONF-2018-006, 2018, URL: https://cds.cern.ch/record/2314418 (cit. on p. 12).

[63] ATLAS Collaboration, *Performance of Missing Transverse Momentum Reconstruction in ATLAS studied in Proton–Proton Collisions recorded in 2012 at* $\sqrt{s}$ = 8 *TeV*, ATLAS-CONF-2013-082, 2013, URL: https://cds.cern.ch/record/1570993 (cit. on p. 12).

[64] ATLAS Collaboration, *Luminosity determination in pp collisions at* $\sqrt{s}$ = 13 *TeV using the ATLAS detector at the LHC*, ATLAS-CONF-2019-021, 2019, URL: https://cds.cern.ch/record/2677054 (cit. on p. 12).

[65] G. Avoni et al., *The new LUCID-2 detector for luminosity measurement and monitoring in ATLAS*, JINST **13** (2018) P07017 (cit. on p. 12).

[66] S. Dulat et al., *New parton distribution functions from a global analysis of quantum chromodynamics*, Phys. Rev. **D93** (2016) 033006, arXiv: 1506.07443 [hep-ph] (cit. on p. 17).

[67] ATLAS Collaboration, *ATLAS Computing Acknowledgements*, ATL-GEN-PUB-2016-002, URL: https://cds.cern.ch/record/2202407 (cit. on p. 23).